Ore Geology Reviews 91 (2017) 264–277

Contents lists available at ScienceDirect

Ore Geology Reviews

journal homepage: www.elsevier.com/locate/oregeorev

Geology, geochemistry and genesis of the Makou magnetite-apatite deposit in the Luzong volcanic basin, Middle-Lower Yangtze River Valley Metallogenic Belt, Eastern China

Liqing Nie[a,b], Taofa Zhou[a,b,*], Yu Fan[a,b], Lejun Zhang[c], David Cooke[c], Noel White[a,b]

[a] School of Resources and Environmental Engineering, Hefei University of Technology, Hefei 230009, China
[b] Ore Deposit and Exploration Centre (ODEC), Hefei University of Technology, Hefei 230009, China
[c] Centre of Excellence in Ore Deposits (CODES), University of Tasmania, Private Bag 79, Hobart, Australia

ARTICLE INFO

Keywords:
MLYB
Luzong Basin
Makou magnetite-apatite iron deposits
zircon U-Pb ages
Albite alteration
Biotite diorite

ABSTRACT

The Middle-Lower Yangtze River Valley Metallogenic Belt (MLYB) is located on the northern margin of the Yangtze Plate (Eastern China). Ore deposits in the belt are mainly clustered in seven ore districts, and are closely associated with Mesozoic intermediate-felsic magmatic rock. Among the seven ore districts, the Luzong and Ningwu districts host large-scale iron resources in volcanic basins. The Makou magnetite-apatite deposit in the southern Luzong Basin was previously interpreted to be related to a quartz syenite porphyry. In this study, we conducted field geological studies and determined the age and geochemistry of the Makou intrusive rocks. Petrography and electron probe micro analysis (EPMA) indicated that the Makou ore-hosting rocks have intense albite alteration. The wallrock alteration is spatially restricted, and comprises albite alteration (Stage I), magnetite mineralization (Stage II), quartz-sulfide alteration (Stage III) and carbonate alteration (Stage IV) stages. Fluid inclusions in syn-mineralization apatite homogenized at 252.2–322.6 °C, which slightly lower than is typical for magnetite-apatite deposits in the region. Field study revealed that the quartz syenite porphyry at Makou disrupted the orebodies along clear-cut intrusive contacts, and that the quartz syenite porphyry does not contain iron mineralization, suggesting it has no direct genetic relationship with the iron mineralization. The ore-hosting albitite and ore-forming biotite diorite have LA-ICP-MS zircon U-Pb ages of 129.6 ± 1.2 Ma and 131.2 ± 3.3 Ma, respectively, and the iron mineralization was dated by mass spectrometer phlogopite ^{40}Ar-^{39}Ar at 130.76 ± 0.77 Ma. We propose that the Makou magnetite-apatite deposit is genetically related to the biotite diorite, rather than to the quartz syenite porphyry in the mine pit. The biotite diorite closely resembles intrusions related to magnetite-apatite deposits elsewhere in the region.

1. Introduction

The Middle-Lower Yangtze River Valley Metallogenic Belt (MLYB), situated at the northern margin of the Yangtze Craton in eastern China, is an important metallogenic province in China (Fig. 1). The belt experienced multiple stages of tectonic, magmatic and ore-forming activity, which were closely related to regional uplift and volcanic basin formation (e.g., Chang et al., 1991; Ren et al., 1991; Zhai et al., 1992; Zhou et al., 2007, 2008, 2010, 2011; Yuan et al., 2008; Fan et al., 2008; Mao et al., 2011). Most ore deposits in the MLYB are located in seven ore districts, namely (from west to east) Edong, Jiurui, Anqing-Guichi, Luzong, Tongling, Ningwu and Ningzhen. Among these districts, Luzong and Ningwu are located in an upwarping zone and host Cu-Au resources, whereas Edong is located in the transition between an upwarping zone and a volcanic basin, and hosts Fe-Cu and Au resources.

Iron deposits of the MLYB are commonly hosted in pyroxene diorite porphyry or along the contact between intrusions and sedimentary rocks, and also locally within the volcanic or sedimentary rocks. Early research had termed these deposits “magnetite-apatite deposits” (Ningwu Iron Ore Research Group, 1978) which is an equivalent of magnetite-apatite deposit (Mao et al., 2008; Li, 2015). It is believed that the magnetite-apatite deposits are closely related to several types of magmatic rocks, such as (pyroxene) diorite (e.g., Geordie and Foster, 2000; Fan et al., 2010; Williams et al., 2005), granitoids (Badham and Morton, 1976; London, 1992; Wolf and London, 1995), meta-volcanics (Zhao and Zhou, 2011) and monzonite/syenite (Ghasem et al., 2012). Most of the magnetite-apatite deposit or magnetite-apatite deposits in

* Corresponding author at: School of Resources and Environmental Engineering, Hefei University of Technology, Hefei 230009, China.
E-mail address: tfzhou@hfut.edu.cn (T. Zhou).

http://dx.doi.org/10.1016/j.oregeorev.2017.09.022
Received 29 April 2017; Received in revised form 16 September 2017; Accepted 29 September 2017
Available online 30 September 2017

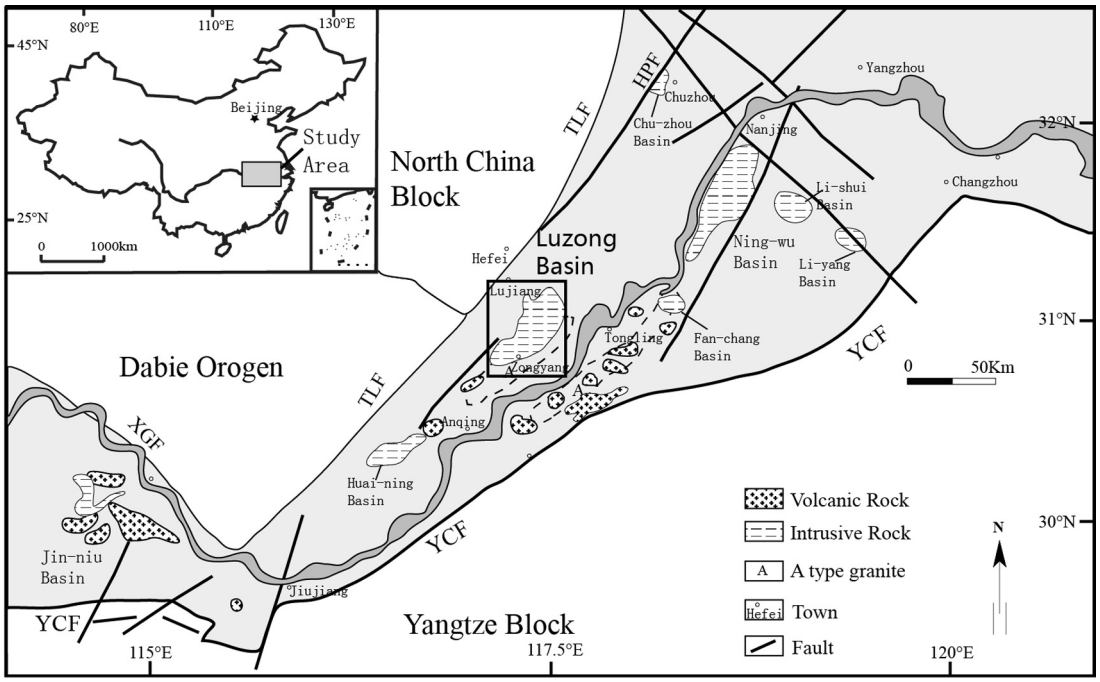

Fig. 1. Sketch map showing the regional geology and the location of volcanic basins in the Middle-Lower Yangtze River Valley Metallogenic Belt (after Zhou et al., 2008).

MLYB are regarded to be related to (pyroxene) diorite (Ningwu Iron Ore Research Group, 1978; Mao et al., 2008; Zhang et al., 2011) except some deposits such as the Makou iron deposit which was thought to be associated with syenite. (Zhang et al., 2014).

Previous work (Zhang et al., 2014) concluded that the quartz syenite porphyry intrusion in the Makou deposit was the source of the ore, making the deposit distinctly different from typical magnetite-apatite deposits. The Makou deposit is associated with intense feldspar alteration of the wall rocks. Previous investigation of the albite alteration at Makou was limited. Some previous works misidentified the albite alteration as K-feldspar alteration, and intensely albite-altered volcanic rocks as “syenite intrusions”. There is a widespread occurrence of strong albite-altered rocks in iron ore deposits in the Luzong Basin. This has caused a lot of confusion and misunderstanding in the study of the genesis and mineralization in the area. The Makou magnetite-apatite deposit is considered to be the product of another period of iron mineralization related to quartz syenite porphyry, which is later than the iron deposits such as Nihe and Luhe deposits in the Luzong basin that formed at 130 Ma (Fan et al., 2014; Zhou et al., 2012a,b) and related to porphyritic diorite. In this study, we conducted detailed field geological mapping, EPMA, whole-rock geochemical analyses, as well as zircon U-Pb and phlogopite Ar-Ar dating. Combining with previous findings (Zhou et al., 2012a,b), we constrained the types and ages of the ore-hosting wall rocks of Makou deposit, compared Makou deposit with typical magnetite-apatite deposits in the region, and discussed the relationship between iron mineralization and quartz syenite porphyry.

2. Regional geology

The Mesozoic continental volcanic basin is controlled by four deep faults (Fig. 2; Ren et al., 1991). The exposed volcanics (800 km^2) are in unconformable contact with the Middle Jurassic Luoling Formation terrestrial clastic sediments. Volcanics in the basin were divided into four volcanic cycles (from old to young): the Longmenyuan, Zhuanqiao, Shuangmiao and Fushan formations. They are exposed in a syncline and each separated from one another along an unconformity. Each volcanic cycle commenced with an eruptive facies, which was followed by increasing lava flows and ended in a volcanic-sedimentary facies (Ren et al., 1991; Zhou et al., 2008). The volcanic eruptions were interpreted to have evolved from fissure-central vent style to typical central vent style, with rock types comprising lavas and volcaniclastic rocks (volcaniclastics more abundant than lavas) (Fig. 2).

The approximately 40 intrusive bodies in the Luzong basin are intimately related to the regional volcanism (Fig. 2). These intrusions comprise mainly (1) monzonite (in northern Luzong basin), with larger ones represented by the Bajiatan, Longqiao and Luoling plutons; (2) syenite, with larger ones represented by the Tudishan and Fenghuangshan plutons; (3) A-type granite, with larger ones including the Chengshan, Huashan and Huangmeijian plutons (Zhou et al., 2007, 2010; Fan et al., 2008).

The Luzong basin is endowed with Au, Cu, Fe, Pb, Zn, U, S and alunite deposits (Fig. 2). The porphyry-type Shaxi Cu-(Au) and Donggushan W deposits were discovered in the northern side of the basin. Major deposit types in the basin include: (1) Zhuanqiao volcanic cycle-related magnetite-apatite deposits (e.g., Luohe, Longqiao, Nihe, Xiaoling and Dabaozhuang), high-sulfidation alunite (e.g., Fanshan) and intermediate-sulfidation Cu-Au deposits (e.g., Jingbian-Shimen’an, Tiantoushan, Bamaoshan); (2) Syenite intrusion-related Fe-oxide-Cu-Au-(U) deposits (e.g., Yangqiao, Wuqiao, 3440 and 34).

3. Ore deposit geology

3.1. Stratigraphy

The stratigraphy includes mainly the Lower Cretaceous Zhuanqiao Formation volcanics distributed to the west of the orebody and Quaternary sediments distributed outside the ore body (Fig. 3). Volcanic rocks contain mainly purplish-grey to dark-grey, vesicular/massive/porphyritic trachyandesite and tuffaceous siltstone (Fig. 4a and b). The trachyandesite contains mainly plagioclase and pyroxene. Plagioclase (oligoclase) grains are largely euhedral (0.5–2 mm), sericitized with occasional corroded margins. Diopside is pale yellowish green (0.05–0.2 mm). Accessory minerals include apatite and magnetite, and the groundmass comprises subhedral plagioclase. Quaternary sediments include humic soil, sandy clay and gravels.

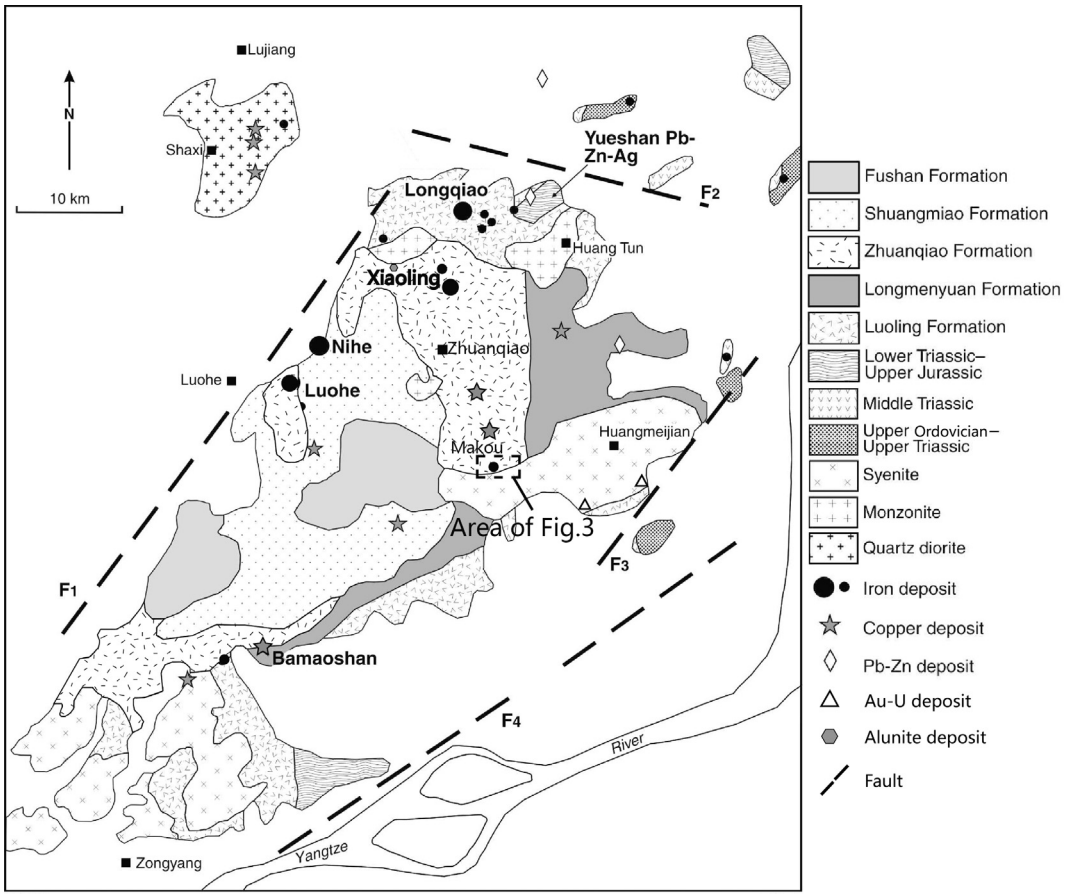

Fig. 2. Simplified geologic map of the Luzong basin, showing the distribution of major ore deposits (after Zhou et al., 2008).

3.2. Structures

Faults are the major structures at Makou. Fault F1 was identified as the ore-controlling structure by field investigation. F1, with well-developed striations and slickensides, is a steeply (72°) SW-dipping extensional shear in quartz syenite porphyry. The northern (220 m long) and southern (250 m long) parts of the fault are exposed, whereas the middle part is covered by Quaternary sediments. Diaclases are well-developed along the shear bands with cleavage planes.

3.3. Igneous rocks

The main intrusive rock in the mine is the Makou pluton and our field and petrographic studies indicate that the pluton is composed of

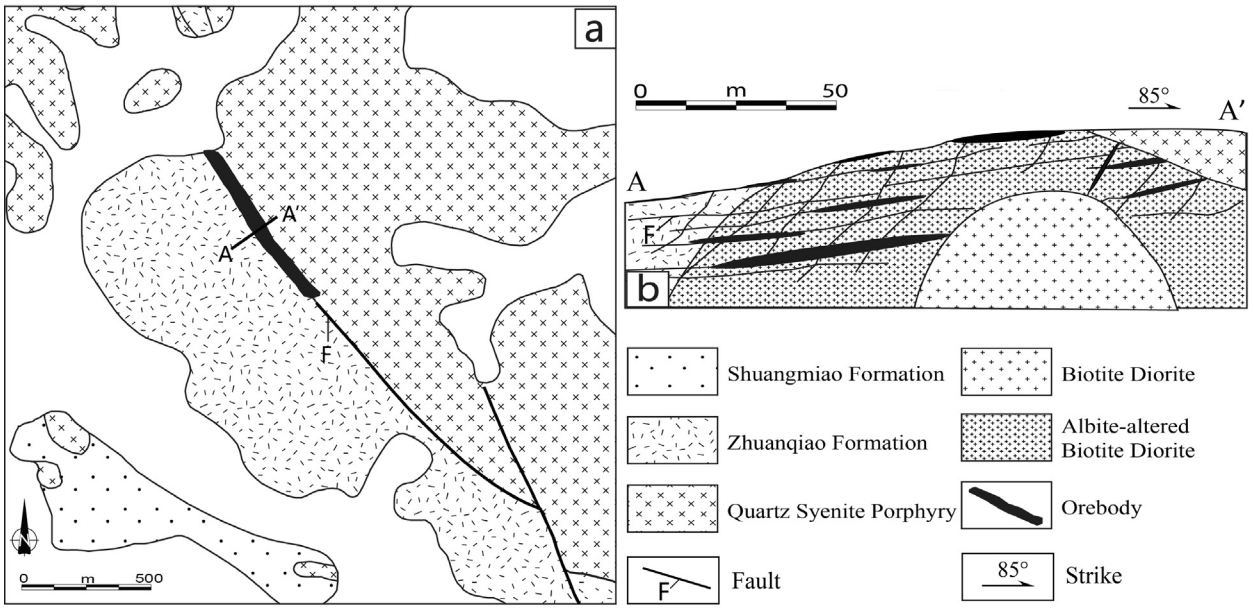

Fig. 3. Geologic map (left) and cross section (right) of the Makou magnetite-apatite deposit.

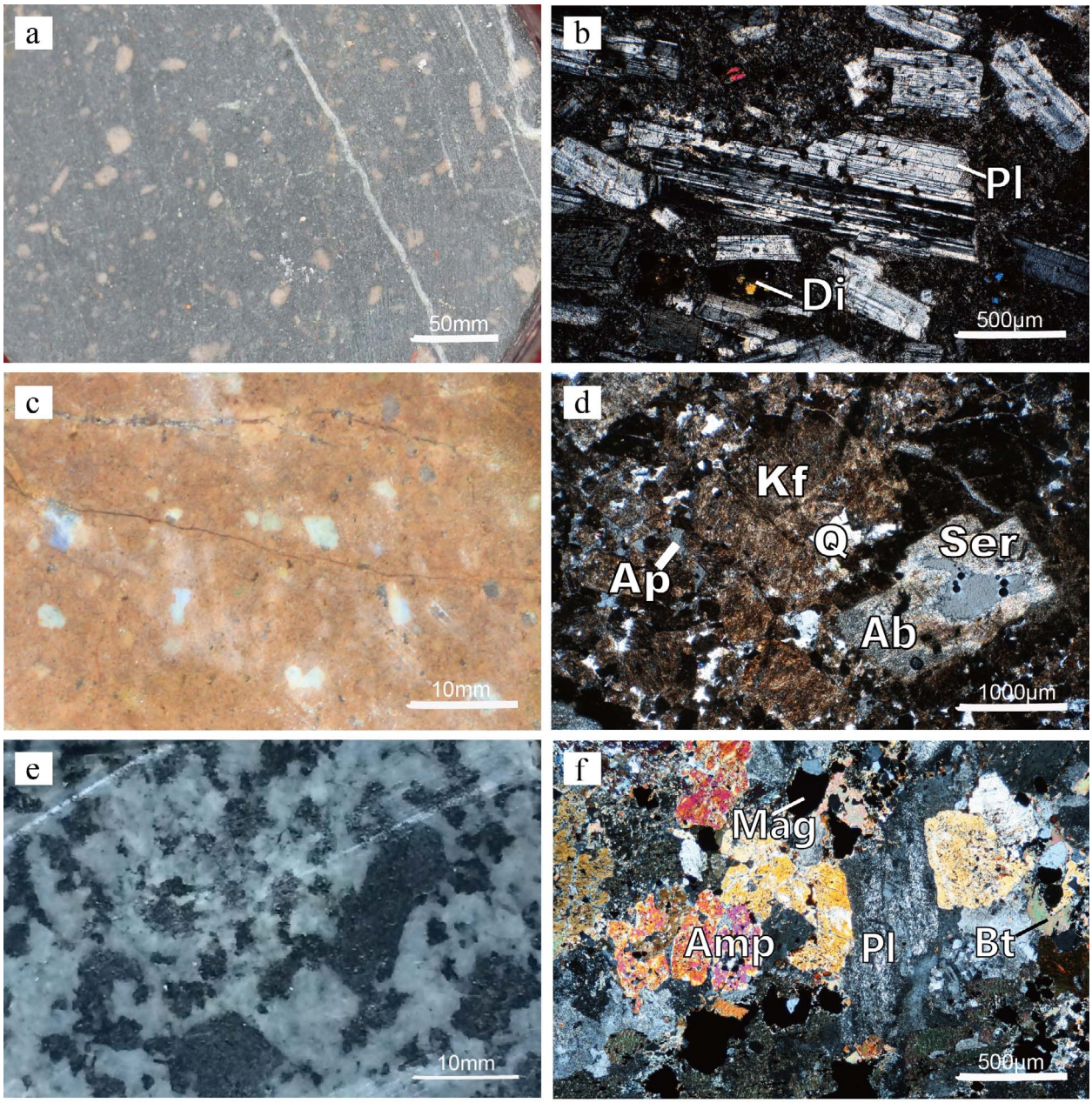

Fig. 4. photomicrographs of the Makou magnetite-apatite deposit: (a) hand specimen and (b) thin section photomicrograph of the Zhuanqiao Formation trachyandesite; (c) hand specimen and (d) thin section photomicrograph of the quartz syenite porphyry; (e) hand specimen and (f) thin section photomicrograph of the biotite diorite. (Pl – Plagioclase; Di – Diopside; Kf – Potassium feldspar; Q – Quartz; Ap – Apatite; Ser – Sericite; Ab – Albite; Mag – Magnetite; Amp – Amphobole; Bt – Biotite).

quartz syenite porphyry (Fig. 4c) which intruded and disrupted the orebody along a clear-cut contact. The rocks are massive (Fig. 4d) and contain mainly K-feldspar (55%), albite (30%) and quartz (10%), with accessory minerals (5%) including apatite and zircon. Sericite alteration is strong and the simple-twinned K-feldspar (0.5–1 mm) appears cloudy due to alteration, whilst the albite (1–5 mm phenocrysts) is largely altered. Anhedral quartz (0.5 mm) occurs interstitially among feldspar grains.

Biotite diorite outcrops were found in a pluton 500 m SE of Makou (Fig. 4e), and consist of plagioclase (40%), amphibole (30%), biotite (20%), magnetite (5%), and quartz (5%) (Fig. 4f). Microscopy petrography showed alteration rims around feldspar phenocrysts. Amphibole (0.1–0.6 mm) is brownish green, whilst plagioclase (0.1–0.8 mm) is albite altered and colorless.

3.4. Wall rock alteration and mineralization

Wall rock alteration at Makou is intense, and comprises dark and light alterations. The dark alteration (Fig. 5a) is represented by magnetite, diopside, chlorite and phlogopite (Fig. 5b), while the light alteration (Fig. 5c) is constituted by albite, calcite and minor K-feldspar (Fig. 5d). The ore-hosting wall rocks are largely albite-altered to become albitite. The rocks are fleshy red, massive and medium to fine-grained crystalline, and contain predominantly albite (95%) and trace amount (5%) of quartz and magnetite. The albite (0.4 mm) is colorless, twinned and appears spotty. Anhedral quartz occurs as interstitials among feldspar grains.

The Makou is a medium scale deposit (> 1.0 million metric tonnes (Mt)). The iron orebodies are in general layered up to 250 m long and

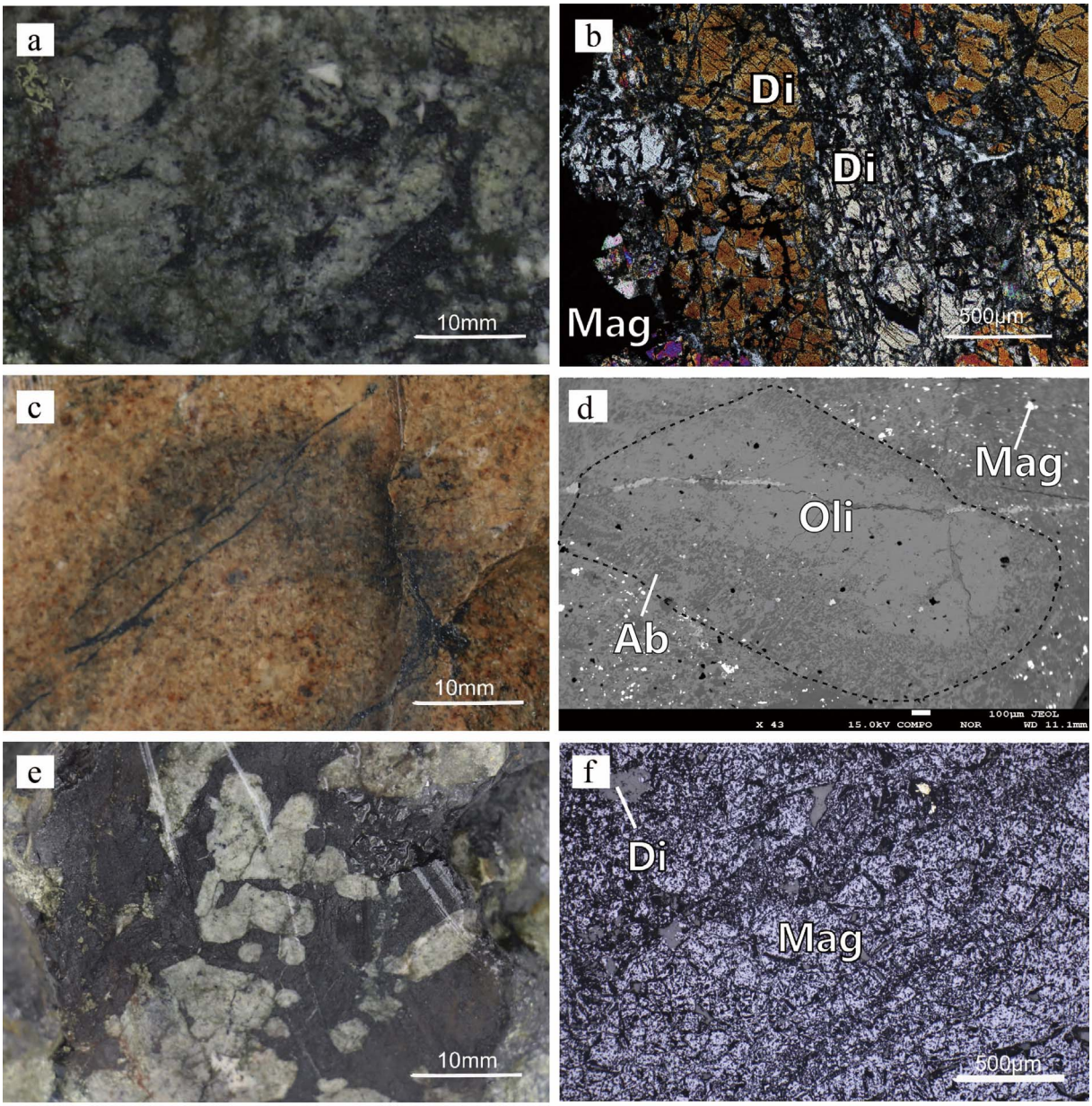

Fig. 5. Mineralization and alteration photomicrographgraphs at Makou: (a) Field and (b) thin section photomicrograph of the Diopside-Apatite-Magnetite altered rock; (c) Field and (d) thin section photomicrograph of the Albite-altered biotite diorite; (e) Field and (f) thin section photomicrograph of the magnetite ore rock. (Di – Diopside; Mag – Magnetite; Ab – Albite; Ap – Apatite).

5.1 m thick, extending 50 m down-dip and contain two types of ores. The iron ores above the albite (Na-altered) trachyandesite contact appear as thin layers, veins or stockworks (vein widths: 5–50 cm), whose orientations are strictly controlled by fracture zones, whilst those in the lower part of the albitite appear as thick massive magnetite layers, and intense albite alteration occurs along the ore veins.

Major ore minerals at Makou include magnetite (Fig. 5e), pyrite, chalcopyrite, hematite and minor specularite, whereas major non-metallic minerals are albite, K-feldspar, diopside, and minor apatite, biotite, phlogopite, sericite, calcite, dolomite, talc, chlorite, quartz, rutile and titanite. Magnetite grains (0.01–0.50 mm) are mainly fine-grained subhedral and minor euhedral (Fig. 5f). Magnetite in veins/stockworks was formed by filling or replacement, and a small amount of ilmenite was found in and around magnetite fractures. The magnetite grains in veins/stockworks are generally coarser than those in disseminations, and show some alteration to specularite.

3.5. Mineralization stages

The Makou alteration/mineralization can be divided into: Stage I: Albite alteration; Stage II: Magnetite mineralization; Stage III: Quartz-sulfide alteration; Stage IV: Carbonate alteration (Fig. 6).

Stage I: Albite alteration: The whole Makou area has alteration, but to different extents. The alteration in the shallow area is weaker than deep area. We identify this kind of alteration by petrography and feldspar dyeing. Primary plagioclase has been partially altered to albite.

Stage II: Magnetite mineralization: The magnetite ore body forming the mining area is lenticular and lens shaped. The structure of the ore is massive, disseminated, vein and net vein. The texture of the ore is mainly hypidiomorphic and xenomorphic granular. The mineral assemblage with magnetite is mainly phlogopite, apatite, diopside and also anhydrite.

Stage III: Quartz-sulfide alteration: The sulfide overprints the magnetite ore body as a quartz sulfide vein. The mainly quartz-sulfide

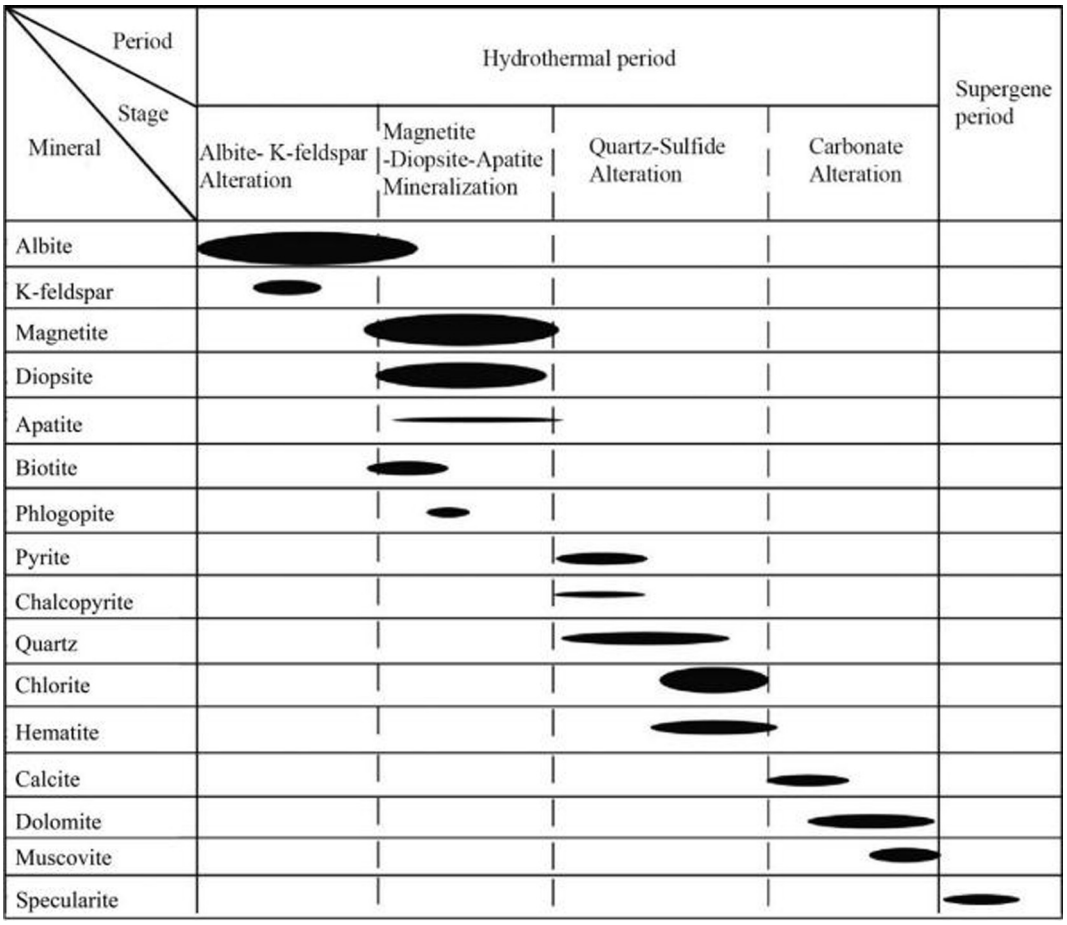

Fig. 6. Mineralization and alteration stages and minerals of the Makou magnetite-apatite deposit.

alteration minerals are pyrite, chalcopyrite, quartz calcite and little anhydrite.

Stage IV: Carbonate alteration is the latest stage of hydrothermal activity. The mainly mineral are carbonate, quartz, hematite (specularite) and a trace pyrite.

4. Geochemistry

4.1. Feldspar and amphibole compositions

In this study, electron probe microanalysis (EPMA) was performed on the feldspar and amphibole from the Makou albitite and biotite diorite. The analyses were conducted at the EPMA laboratory of the Hefei University of Technology (HFUT). Analytical conditions: Machine model: JXA-8230 Acceleration voltage: 15 kV; Current: 20 nA; Beam size: 3 μm. Standards used were the SPI 53 minerals standard. Data correction was performed by the PRZ method, analytical accuracy was 1–5%.

EPMA data indicate that plagioclase from the Makou albitite contains An compositions of 1.04–38.73, with 86.21% of the samples falling into the albite field (Fig. 7; Table 1). Plagioclase from the Makou biotite diorite contains An compositions of 1.19–50.01. A small amount of K-feldspar contains Or compositions of 90.14–94.78 (Fig. 8; Table 2). Amphibole from the Makou biotite diorite contains $^{B}(Mg^{2+} + Fe^{2+} + Mn^{2+} + Li^{+}) = 0.00–0.03 \leq 0.50$, $^{B}(Ca + Na) = 1.97–2.00 \geq 1.00$ and $^{B}Na = 0.12–0.19 < 0.50$, and thus belongs to Ca-amphibole. The $^{B}Ca = 1.50–1.86 \geq 1.50$ suggests that the amphibole is diopside (Fig. 9; Table 3).

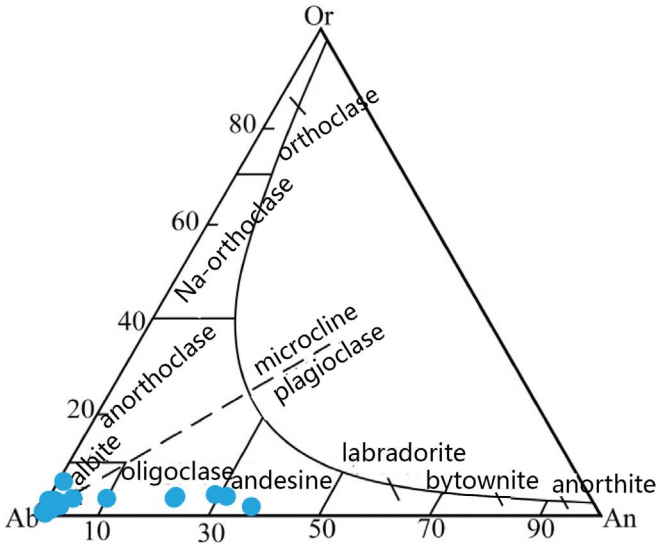

Fig. 7. Classification diagram for the feldspars from the Makou albitite.

4.2. Whole rock geochemistry

In this study we selected fresh biotite diorite and quartz syenite porphyry from Makou area (Table 4), which have the characteristics described above. The whole rock major and trace element analyses were carried out at the ALS Global Analytical Company, Guangzhou, China. Major elements were analyzed using X-ray fluorescence

Table 1
EPMA results of the Feldspars from the Makou albitite (wt%).

Sample	SiO_2	Al_2O_3	CaO	Na_2O	K_2O	Si	Al	Ca	Na	K	An	Ab	Or
ZK376-2	68.805	18.977	0.195	11.114	0.075	3.0212	0.9821	0.0092	0.9462	0.0042	0.96	98.61	0.44
ZK376-1	68.783	19.046	0.216	11.256	0.092	3.0162	0.9843	0.0101	0.9570	0.0051	1.04	98.43	0.53
MK15-1	69.104	18.867	0.446	10.384	0.422	3.0313	0.9754	0.0210	0.8832	0.0236	2.26	95.20	2.55
MK15-2	68.581	18.970	0.513	10.695	0.306	3.0177	0.9838	0.0242	0.9124	0.0172	2.54	95.66	1.80
MK17-1	60.711	24.058	6.423	7.194	0.672	2.7249	1.2726	0.3089	0.6260	0.0385	31.73	64.31	3.95
MK17-2	61.160	23.796	5.889	7.372	0.707	2.7442	1.2584	0.2831	0.6413	0.0405	29.34	66.46	4.19
MK13-1	66.343	20.263	2.145	9.777	0.622	2.9375	1.0574	0.1018	0.8393	0.0351	10.42	85.98	3.60
MK13-2	61.160	23.796	5.889	7.372	0.707	2.7442	1.2584	0.2831	0.6413	0.0405	29.34	66.46	4.19
ZK314-1	63.027	22.450	4.574	8.141	0.670	2.8174	1.1828	0.2191	0.7056	0.0382	22.75	73.28	3.97
ZK314-2	62.902	22.518	4.627	8.356	0.614	2.8103	1.1857	0.2215	0.7238	0.0350	22.59	73.84	3.57
ZK314-3	67.482	19.723	0.947	10.316	0.588	2.9790	1.0261	0.0448	0.8830	0.0331	4.66	91.89	3.45
MK4-1	66.768	18.351	0.134	11.763	0.153	3.0072	0.9741	0.0065	1.0272	0.0088	0.62	98.54	0.84
MK4-2	65.755	18.195	0.125	10.968	0.158	3.0138	0.9829	0.0061	0.9747	0.0092	0.62	98.45	0.93
MK-3-3	70.101	18.446	0.104	11.306	0.164	3.0481	0.9453	0.0048	0.9531	0.0091	0.50	98.56	0.94
MK-3-3	69.562	18.666	0.137	11.524	0.109	2.7442	1.2584	0.2831	0.6413	0.0405	38.73	58.08	3.19
MK-10-2	69.636	18.661	0.416	11.188	0.272	3.0321	0.9577	0.0194	0.9445	0.0151	1.98	96.47	1.54
MK-10-2	70.856	18.509	0.337	11.311	0.328	3.0481	0.9384	0.0155	0.9434	0.0180	1.59	96.57	1.84
MK-10-1	69.290	18.637	0.245	10.381	1.158	3.0358	0.9624	0.0115	0.8818	0.0647	1.20	92.04	6.76
MK-10-1	70.637	18.722	0.606	11.200	0.368	3.0363	0.9485	0.0279	0.9334	0.0202	2.84	95.10	2.06
MK-7-3	69.065	18.710	0.419	11.360	0.255	3.0220	0.9649	0.0196	0.9638	0.0142	1.97	96.60	1.43
MK-7-3	69.073	18.631	0.302	11.306	0.218	3.0278	0.9625	0.0142	0.9609	0.0122	1.44	97.33	1.23
MK-7-3	71.552	18.703	0.315	10.963	0.518	3.0535	0.9407	0.0144	0.9071	0.0282	1.52	95.51	2.97
MK-7-3	71.670	18.723	0.280	11.356	0.281	3.0510	0.9394	0.0128	0.9373	0.0153	1.32	97.10	1.58
MK-11-3	70.207	18.654	0.372	11.593	0.235	3.0330	0.9498	0.0172	0.9711	0.013	1.72	96.99	1.29
MK-11-3	68.709	18.069	0.176	11.359	0.294	3.0411	0.9425	0.0083	0.9748	0.0166	0.83	97.50	1.66
MK-11-4	69.148	17.693	0.188	11.150	0.221	3.0609	0.9231	0.0089	0.9570	0.0125	0.91	97.81	1.28
MK-11-4	68.205	17.759	0.212	10.901	0.226	3.0526	0.9368	0.0102	0.9460	0.0129	1.05	97.62	1.33
MK-14-3	70.964	18.211	0.079	11.449	0.107	3.0625	0.9263	0.0037	0.9580	0.0059	0.38	99.01	0.61
MK-14-3	69.338	18.137	0.118	11.217	0.515	3.0467	0.9392	0.0056	0.9556	0.0289	0.56	96.52	2.92

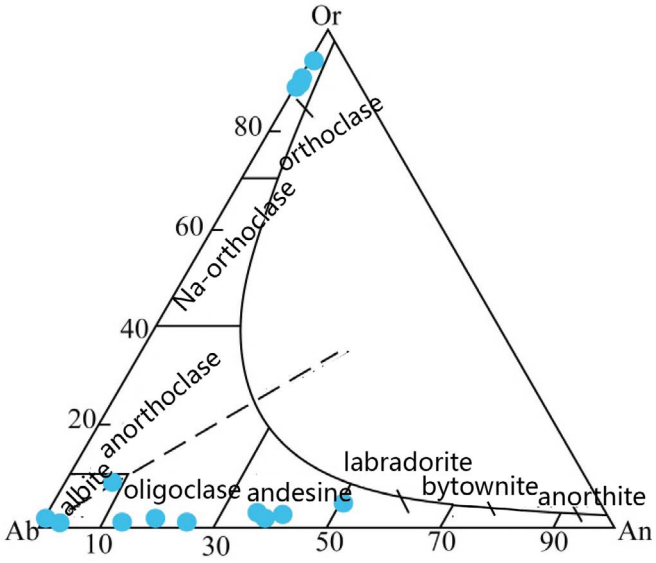

Fig. 8. Classification diagram for the feldspars from the Makou biotite diorite.

spectroscopy (Norrish and Chappell, 1977). Ferric and ferrous iron ratios were determined by wet chemical methods. Trace element abundances, including the rare earth elements (REE), were determined by ICP-MS with a Finnegan MAT Element II mass spectrometer. The samples were digested with a mixture of HF and HNO_3 acids in screw-top PTFE-lined stainless steel bombs at 185 °C for 48 h, and any residues were dissolved in HNO3 at 145 °C for 3 h to ensure complete digestion. Details of the analytical method used are described by Dulski (1994). Analysis of the Chinese basalt standard GSR-3 (Xie et al., 1989) indicates that the precision and accuracy of the major-element data are better than 3% and ca. 5% (2 sigma), respectively. The analytical precision of ICP-MS analysis was better than ± 5% based on analysis of the USGS BHVO-1 standard.

4.3. Ore fluid characteristics

4.3.1. Fluid inclusion types and features

According to the alteration/mineralization stages, Stage II apatite and Stage III quartz were chosen for the fluid inclusion (FI) analysis. Fluid inclusions are rare in Stage III quartz, and consist mainly of vapor-liquid (two phase) under room temperature. The FIs (< 5 μm long) appear as rounded, negative crystal or irregular shapes, and occur either as isolated FIs or in clusters. No healed fractures are present around these FIs, suggesting that they are mainly primary (Fig. 10a and b). Fluid inclusions are well-developed in Stage II apatite, and are mainly vapor-liquid FIs (no daughter minerals). Some FIs (< 10 μm long) are irregular or ellipsoidal and isolated (Fig. 10c), and others are tabular or needle-shaped (5–10 μm long, 2–3 μm wide) (Fig. 10d).

4.3.2. Microthermometry

The FI microthermometric analysis was conducted at the School of Resources and Environmental Engineering (HFUT) via homogeneity and freezing method (Lu, 1990), using a Linkam THMS600 heating/cooling stage (−196 to 600 °C). Results (< 0.1 °C temperature difference) indicate that the FIs from Stage II apatite homogenized at 252.2–322.6 °C (average 279 °C), whereas those from Stage III quartz homogenized at 120.1–189.2 °C (average 163.1 °C). The homogenization temperatures are lower than those from apatite in the Ningwu area (Ma et al., 2006), as well as those from the ore-fluids of the Nihe and Luohe porphyrite-type iron deposits in the Luzong basin.

5. Magmatic and mineralization ages

5.1. Methods

Fresh biotite diorite and albitite from Makou were zircon U-Pb dated (Fig. 11), and phlogopite coexisting with magnetite ores was Ar-Ar dated. Zircons were first separated by conventional crushing, sieving and magnetic separation techniques, and then handpicked under a binocular microscope at the laboratory of the Hebei Regional Geological

Table 2
EPMA results of the feldspars from the Makou biotite diorite (wt%).

Sample	SiO_2	Al_2O_3	CaO	Na_2O	K_2O	Si	Al	Ca	Na	K	Ba	An	Ab	Or
MK75-1	67.63	19.92	0.25	11.24	0.33	2.9752	1.0328	0.0118	0.9587	0.0185	0.0000	1.19	96.94	1.87
MK75-2	63.09	21.95	8.37	7.19	0.35	2.7864	1.1425	0.3960	0.6153	0.0196	0.0000	38.41	59.69	1.90
MK75-3	58.29	25.80	7.50	6.88	0.53	2.6313	1.3723	0.3625	0.6025	0.0305	0.0000	36.41	60.52	3.07
MK78-1	54.90	27.00	9.44	7.23	0.49	2.5103	1.4549	0.4625	0.6407	0.0285	0.0000	40.87	56.61	2.52
MK78-2	60.64	19.70	0.00	1.16	15.95	2.8980	1.1093	0.0000	0.1073	0.9727	0.0000	0.00	9.94	90.06
MK78-3	53.14	27.54	10.85	5.42	0.88	2.4662	1.5059	0.5392	0.4872	0.0519	0.0000	50.01	45.18	4.81
MK78-4	63.63	17.76	0.00	1.23	15.34	3.0008	0.9871	0.0000	0.1125	0.9229	0.0000	0.00	9.86	90.14
MK77-1	63.00	21.10	3.29	10.75	0.19	2.8415	1.1216	0.1590	0.9401	0.0109	0.0000	14.32	84.69	0.98
MK77-2	64.14	20.62	0.00	11.14	0.05	2.9227	1.1074	0.0000	0.9842	0.0029	0.0000	0.00	99.71	0.29
MK77-3	60.95	24.23	5.78	9.28	0.25	2.7076	1.2686	0.2751	0.7993	0.0142	0.0000	25.27	73.43	1.30
MK76-1	62.04	23.16	4.50	9.91	0.34	2.7624	1.2154	0.2147	0.8555	0.0193	0.0000	19.70	78.52	1.77
MK76-2	65.04	17.80	0.00	0.59	16.29	3.0162	0.9729	0.0000	0.0530	0.9637	0.0000	0.00	5.22	94.78
MK76-3	64.71	17.73	0.00	0.98	15.42	3.0177	0.9745	0.0000	0.0886	0.9174	0.0000	0.00	8.81	91.19

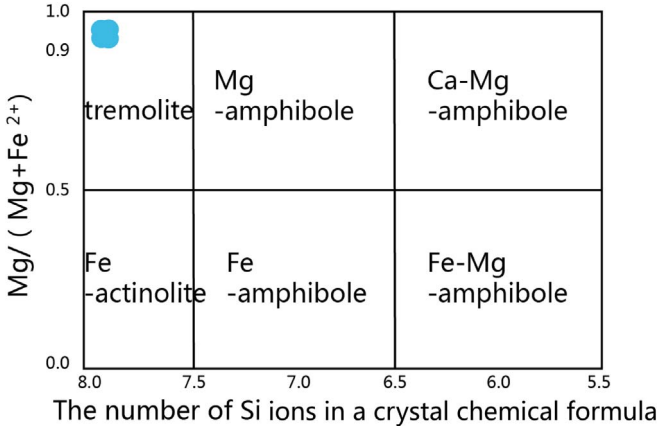

Fig. 9. Classification diagram of the amphibole from the Makou biotite diorite.

Survey Institute. Euhedral and transparent zircons were chosen and mounted on epoxy. The zircons were polished, studied/imaged first by transmitted and reflected light microscopy and then by cathodoluminescence (CL) imaging.

Representative zircons were U-Pb dated using a GeoLasPro 193 nm ComPex 102ArF laser ablation system coupled with an Agilent 7500a ICP-MS (equipped with Shield Torch) at the School of Resources and Environmental Engineering (HFUT). Analytical conditions: Beam size: 4–160 μm; Energy intensity range: 1–45 J/cm^2; Energy pulse: 200 mJ; Repetition rate: 20 Hz; High purity Ar (carrier gas) and He (compensation gas) (99.999%); ^{204}Pb and ^{202}Hg background $<$ 100 cps. 91,500 standards (Wiedenbeck et al., 1995) were analyzed twice for every five analyses, and NIST 610 and Mud Tank (Black and Culson, 1978) once for every ten analyses. Each analysis comprises a background measurement (20–30 s, usually 25 s) and sample measurement (40–50 s, usually 50 s). Zircon U-Pb concordia plot and weighted average calculation were done using Isoplot/Ex_ver3 (Ludwig, 2003). Analytical uncertainties for the zircon U-Th-Pb isotopic ratios and ages were reported in 1σ, and those of weighted average age in 2σ. The low ^{204}Pb signal and signal interference of ^{204}Hg in the carrier gas mean that ^{204}Pb concentrations cannot be accurately measured, and the EXCEL ComPbCorr#3.18 procedure was conducted for common Pb correction (Andersen, 2002).

The ^{40}Ar/^{39}Ar analyses were performed at the Western Australian Argon Isotope Facility at Curtin University. The samples were step-heated using a 110 W Spectron Laser Systems, with a continuous Nd-YAG (IR; 1064 nm) laser rastered over the sample during 1 min to ensure a homogenously distributed temperature. The gas was purified in a stainless steel extraction line using two SAES AP10 getters, a GP50 getter and a liquid nitrogen condensation trap. Ar isotopes were measured in static mode using a MAP 215–50 mass spectrometer (resolution of ~500; sensitivity of 4×10^{-14} mol/V) with a Balzers SEV 217 electron multiplier mostly using 9–10 cycles of peak-hopping. The data acquisition was performed with the Argus program written by M.O. McWilliams and ran under a Lab View environment. The raw data were processed using the ArArCALC software (Koppers, 2002) and the ages have been calculated using the decay constants recommended by Renne et al. (2010). Blanks were monitored every 3–4 steps and typical ^{40}Ar blanks range from 1×10^{-16} to 2×10^{-16} mol. Samples were loaded into large wells of one 1.9 cm diameter and 0.3 cm depth aluminum disc. These wells were bracketed by small wells that included Fish

Table 3
EPMA results of the amphibole from the Makou biotite diorite (wt%).

Element	MK75	MK77	MK78-1	MK78-2
SiO_2	55.37	55.42	57.19	57.64
Al_2O_3	1.92	1.74	0.73	0.33
CaO	12.24	12.21	10.08	10.00
Na_2O	0.78	0.63	2.66	2.58
K_2O	0.21	0.18	0.65	0.69
MgO	18.04	17.60	19.79	20.15
FeO	8.79	8.79	6.50	6.23
MnO	0.33	0.39	0.06	0.09
Cr_2O_3	0.00	0.01	0.01	0.00
TiO_2	0.19	0.24	0.48	0.17
Total	97.84	97.20	98.15	97.88
Si	7.82	7.87	7.96	8.03
Al(IV)	0.18	0.13	0.04	0.00
Al(VI)	0.14	0.16	0.08	0.08
Ti	0.02	0.03	0.05	0.02
Fe^{3+}	0.87	0.94	0.66	0.67
Fe^{2+}	0.17	0.11	0.10	0.06
Mn	0.04	0.05	0.01	0.01
Mg	3.80	3.73	4.11	4.18
Ca	1.85	1.86	1.50	1.49
Na	0.21	0.17	0.72	0.70
K	0.04	0.03	0.12	0.12
Cation	15.13	15.06	15.34	15.33
OH^-	0.00	0.00	0.00	0.00
F	0.00	0.00	0.00	0.00
Cl	0.00	0.00	0.00	0.00
Si_T^*	7.82	7.87	7.96	8.03
Al_T	0.18	0.13	0.04	0.00
Al_C	0.14	0.16	0.08	0.08
Fe_C^{3+}	0.87	0.94	0.66	0.67
Ti_C	0.02	0.03	0.05	0.02
Mg_C	3.80	3.73	4.11	4.18
Fe_C^{2+}	0.17	0.11	0.10	0.05
Mn_C	0.01	0.05	0.00	
Fe_B^{2+}	0.00	0.00	0.00	0.01
Mn_B	0.03	0.00	0.01	0.01
Ca_B	1.85	1.86	1.50	1.49
Na_B	0.12	0.14	0.49	0.48
Ca_A	0.00	0.00	0.00	0.00
Na_A	0.09	0.03	0.23	0.21
K_A	0.04	0.03	0.12	0.12
Mg#	0.79	0.78	0.84	0.85

Table 4
Major element compositions for the major Makou igneous rocks.

Sample	Lithology	SiO_2	TiO_2	Al_2O_3	Fe_2O_3	CaO	MgO	MnO	Na_2O	K_2O	P_2O_5	LOI	Total
MK72	Biotite diorite	60.10	1.87	16.42	10.67	6.29	4.85	0.25	3.41	3.12	0.98	1.74	100.87
MK11	Na-altered biotite diorite	64.90	0.48	15.20	4.91	1.40	1.40	0.03	7.95	0.30	0.03	2.48	102.44
MK7	Na-altered biotite diorite	66.80	0.52	16.05	2.74	0.98	0.80	0.03	7.99	1.09	0.14	2.07	100.16
ZK501-346	Albitite	64.88	0.88	17.18	0.93	1.86	0.48	0.05	10.15	0.17	< 0.01	2.19	100.78
MK17	Quartz syenite porphyry	67.40	0.45	17.35	1.59	0.32	0.30	0.06	4.18	6.74	0.15	1.04	99.81
MK18	Quartz syenite porphyry	62.30	0.46	16.35	3.77	1.60	0.92	0.07	4.50	6.91	0.10	2.59	100.85
ZK401-221	Trachyandesite	58.34	0.76	15.51	3.22	2.03	1.64	0.11	5.21	4.01	0.47	2.78	99.23
ZK401-200	Trachyandesite	56.41	0.65	14.49	3.08	3.33	1.50	0.13	6.89	3.77	0.36	2.80	99.87

Canyon sanidine (FCs) used as a neutron fluence monitor for which an age of 28.294 ± 0.036 Ma (1σ) was adopted (Renne et al., 2011). The discs were Cd-shielded (to minimize undesirable nuclear interference reactions) and irradiated for 40 h in the US Geological Survey nuclear reactor (Denver, USA) in central position. The mean J-values computed from standard grains within the small pits range from 0.01059100 ± 0.0000040 (0.15%) to 0.01059100 ± 0.000054 (0.20%) determined as the average and standard deviation of J-values of the small wells for each irradiation disc. Mass discrimination was monitored using an automated air pipette and provided a mean value of 1.004396 ± 0.003 per dalton (atomic mass unit) relative to an air ratio of 298.56 ± 0.31 (Lee et al., 2006). The correction factors for interfering isotopes were $(^{39}Ar/^{37}Ar)_{Ca} = 7.30 \times 10^{-4}$ (± 11%), $(^{36}Ar/^{37}Ar)_{Ca} = 2.82 \times 10^{-4}$ (± 1%) and $(^{40}Ar/^{39}Ar)_{K} = 6.76 \times 10^{-4}$ (± 32%). Our criteria for the determination of plateau are as follows: plateaus must include at least 70% of ^{39}Ar. The plateau should be distributed over a minimum of 3 consecutive steps agreeing at 95% confidence level and satisfying a probability of fit (P) of at least 0.05.

5.2. Zircon U-Pb results

Zircon U-Pb data are listed in Table 5 and U-Pb concordia diagrams illustrated in Fig. 12. The zircons analyzed are colorless or pale yellow and tabular prismatic. The zircons also lack inherited cores and metamorphic rims, and the clear igneous oscillatory zoning (Fig. 11). The Th/U data of zircons are from 0.44 to 2.33 which suggest that the zircons are likely magmatic (Belousova et al., 2001) and their ages reflect the rock formation age. The Makou biotite diorite and ore-hosting albitite were zircon U-Pb dated to be 131.2 ± 3.3 Ma (MSWD = 1.7; n = 13) and 129.6 ± 1.2 Ma (MSWD = 0.26; n = 23), respectively.

5.3. Phlogopite Ar-Ar results

Plateau ages are 130.76 ± 0.77 Ma (MSWD = 1.7) (Table 6 and Fig. 13) are given at the 2σ level and are calculated using the mean of all the plateau steps, each weighted by the inverse variance of their

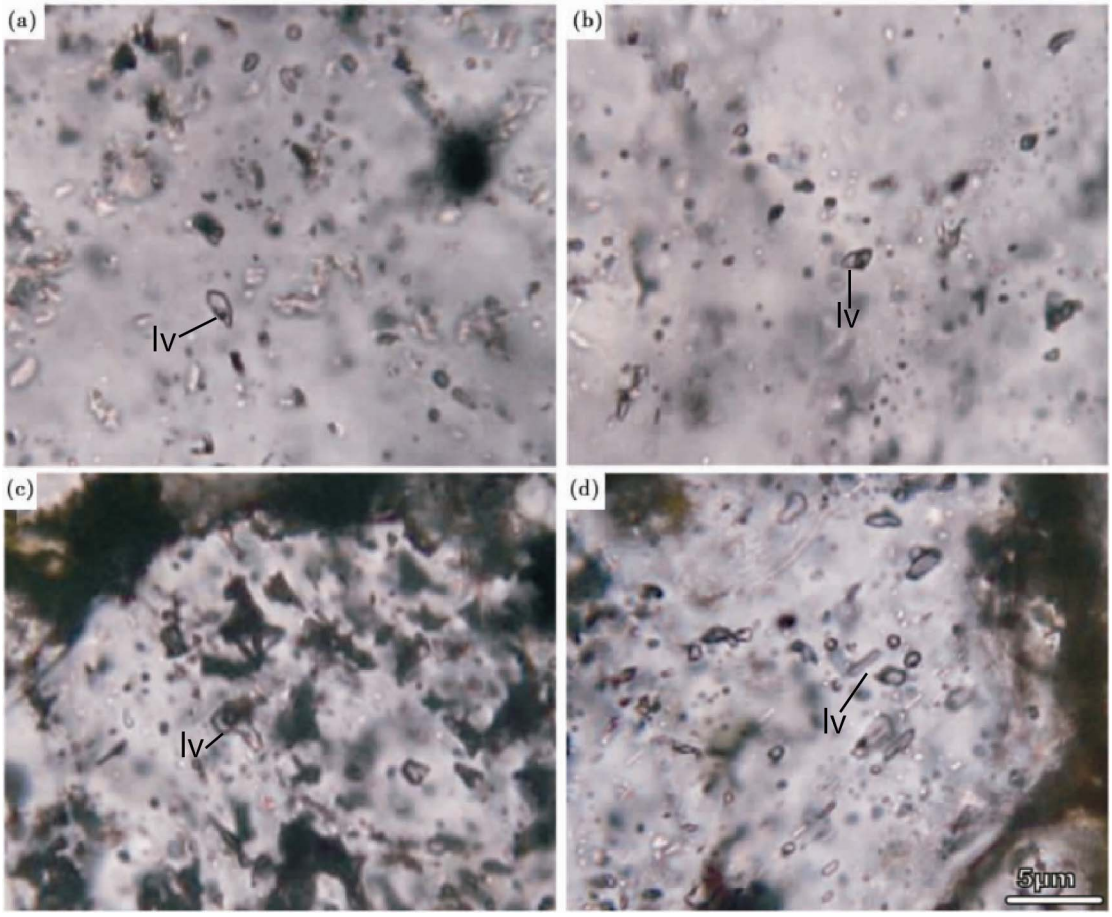

Fig. 10. Fluid inclusion photographs of the Makou (a, b). Stage II apatite; (c, d). Stage III quartz. (lv – vapor-liquid two-phase inclusions).

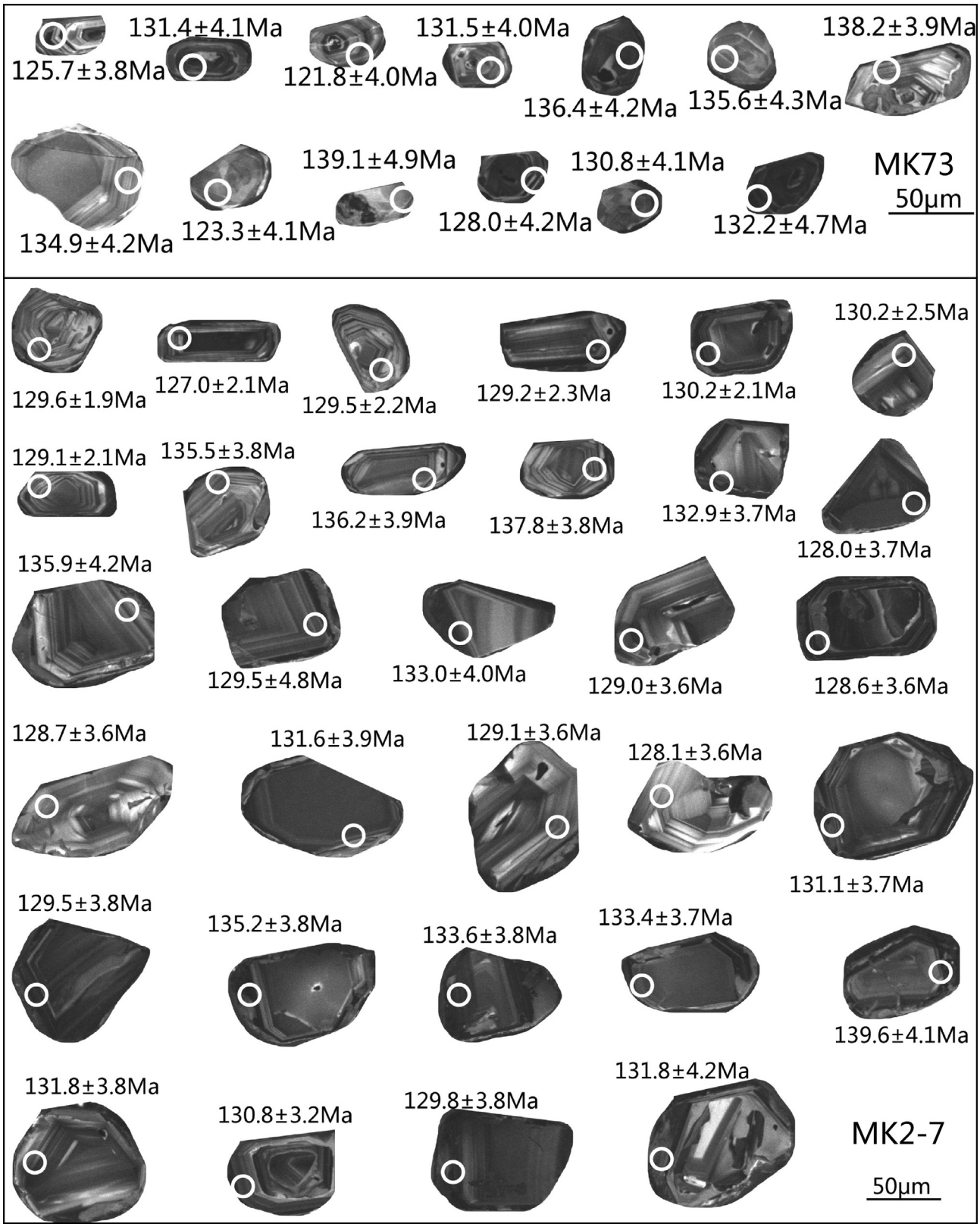

Fig. 11. CL images of zircons from biotite diorite and albitite in Makou area and their data.

individual analytical error. Mini-plateaus are defined similarly except that they include between 50% and 70% of ^{39}Ar. Integrated ages (2σ) are calculated using the total gas released for each Ar isotope. Inverse isochrons include the maximum number of steps with a probability of fit ≥0.05. All sources of uncertainties are included in the calculation.

6. Genesis of the Makou iron mineralization

6.1. Constraints from field geology, mineral and whole-rock geochemistry

In the past, the mineralization-related magmatic rocks were

Table 5
LA-ICP-MS zircon U-Pb dating data of the intrusions from biotite diorite and albitite in Makou area.

Sample	$\times 10^{-6}$		Th/U	$^{207}Pb/^{206}Pb$		$^{206}Pb/^{238}Pb$		$^{208}Pb/^{232}Pb$		$^{206}Pb/^{238}Pb$		$^{207}Pb/^{235}Pb$		$^{208}Pb/^{232}Pb$	
	U	Th		Data	1σ	Data	1σ	Data	1σ	Age (Ma)	1σ	Age (Ma)	1σ	Age (Ma)	1σ
Albitite															
MK2-7-1	1139.4238	875.8162	1.3010	0.0503	0.0032	0.0201	0.0006	0.0073	0.0003	128.0	3.7	133.7	8.1	147.6	6.0
MK2-7-2	950.2814	773.7803	1.2281	0.0486	0.0030	0.0213	0.0007	0.0079	0.0004	135.9	4.2	133.9	7.6	159.2	7.1
MK2-7-3	1385.8148	1498.9621	0.9245	0.0488	0.0026	0.0204	0.0006	0.0068	0.0003	130.0	3.7	130.7	6.4	136.5	5.6
MK2-7-4	509.5758	669.9583	0.7606	0.0541	0.0038	0.0215	0.0007	0.0069	0.0003	136.9	4.2	149.7	9.4	139.3	6.9
MK2-7-5	1202.9344	916.8320	1.3121	0.0477	0.0029	0.0203	0.0006	0.0066	0.0003	129.5	3.8	126.7	7.0	133.9	5.6
MK2-7-6	538.3632	581.8735	0.9252	0.0548	0.0038	0.0209	0.0006	0.0074	0.0003	133.0	4.0	147.0	9.3	148.4	6.4
MK2-7-7	1415.9818	1633.4925	0.8668	0.0507	0.0026	0.0202	0.0006	0.0068	0.0003	129.2	3.6	135.0	6.4	137.6	5.1
MK2-7-8	935.0870	1507.3008	0.6204	0.0448	0.0023	0.0207	0.0006	0.0069	0.0003	131.8	3.8	122.1	5.9	139.3	5.6
MK2-7-9	1992.0937	1173.1979	1.6980	0.0484	0.0027	0.0202	0.0006	0.0064	0.0002	129.0	3.6	129.4	6.9	128.0	4.9
MK2-7-10	854.6224	1362.3746	0.6273	0.0464	0.0026	0.0201	0.0006	0.0060	0.0002	128.6	3.6	123.4	6.4	120.1	4.9
MK2-7-11	1881.6837	1866.5000	1.0081	0.0466	0.0024	0.0202	0.0006	0.0064	0.0002	128.7	3.6	124.2	5.9	129.1	4.7
MK2-7-12	762.5714	595.0900	1.2814	0.0473	0.0032	0.0206	0.0006	0.0070	0.0003	131.6	3.9	127.1	7.6	141.7	5.9
MK2-7-13	1850.0437	1206.2265	1.5337	0.0504	0.0027	0.0202	0.0006	0.0061	0.0002	129.1	3.6	135.2	6.7	122.8	4.7
MK2-7-14	1329.7211	862.5805	1.5416	0.0495	0.0027	0.0201	0.0006	0.0061	0.0002	128.1	3.6	129.9	6.4	123.2	4.7
MK2-7-15	1370.5328	824.9805	1.6613	0.0454	0.0028	0.0205	0.0006	0.0068	0.0003	131.1	3.7	123.7	7.1	137.7	5.3
MK2-7-16	571.9838	449.8180	1.2716	0.0515	0.0032	0.0203	0.0006	0.0065	0.0003	129.5	3.8	136.8	8.0	130.4	5.4
MK2-7-17	966.0404	911.7147	1.0596	0.0502	0.0026	0.0212	0.0006	0.0069	0.0003	135.2	3.8	139.3	6.8	138.6	5.2
MK2-7-18	487.2339	518.6717	0.9394	0.0534	0.0033	0.0209	0.0006	0.0067	0.0003	133.6	3.8	146.9	8.6	135.7	5.4
MK2-7-19	1270.2945	906.1101	1.4019	0.0457	0.0026	0.0209	0.0006	0.0069	0.0003	133.4	3.7	125.3	6.4	139.0	5.1
MK2-7-20	285.7818	432.0596	0.6614	0.0508	0.0034	0.0219	0.0006	0.0074	0.0003	139.6	4.1	143.2	8.4	150.0	6.5
MK2-7-21	945.7789	1284.9927	0.7360	0.0485	0.0026	0.0208	0.0006	0.0068	0.0003	132.9	3.7	132.6	6.4	137.1	5.2
MK2-7-22	1516.6728	1209.9933	1.2535	0.0492	0.0025	0.0216	0.0006	0.0074	0.0003	137.8	3.8	139.2	6.4	148.6	5.4
MK2-7-23	906.5393	807.7875	1.1222	0.0497	0.0031	0.0214	0.0006	0.0072	0.0003	136.2	3.9	138.6	7.6	145.1	5.9
MK2-7-24	1225.1762	922.7289	1.3278	0.0499	0.0026	0.0212	0.0006	0.0069	0.0003	135.5	3.8	138.2	6.4	139.5	5.2
MK2-7-25	671.8418	619.3738	1.0847	0.0499	0.0029	0.0202	0.0003	0.0067	0.0002	129.1	2.1	132.0	7.0	135.7	4.4
MK2-7-26	461.8229	396.6412	1.1643	0.0520	0.0033	0.0204	0.0004	0.0069	0.0002	130.2	2.5	136.9	7.5	139.0	4.8
MK2-7-27	547.4645	419.8749	1.3039	0.0489	0.0030	0.0204	0.0003	0.0066	0.0002	130.2	2.1	129.8	7.0	133.0	4.3
MK2-7-28	362.6079	398.2700	0.9105	0.0530	0.0036	0.0203	0.0004	0.0063	0.0002	129.2	2.3	138.6	8.3	126.2	4.5
MK2-7-29	619.4561	500.9572	1.2365	0.0545	0.0039	0.0203	0.0004	0.0071	0.0002	129.5	2.2	142.2	9.1	143.1	5.0
MK2-7-30	791.5573	499.1811	1.5857	0.0466	0.0028	0.0199	0.0003	0.0065	0.0002	127.0	2.1	121.8	6.7	130.1	3.9
MK2-7-31	1107.4054	814.8517	1.3590	0.0522	0.0026	0.0203	0.0003	0.0067	0.0002	129.6	1.9	138.5	6.4	134.7	3.9
Biotite diorite															
MK73-01	578.4064	1348.1870	2.3309	0.0482	0.0038	0.0207	0.0007	0.0063	0.0003	126.1	3.8	126.4	7.7	121.2	6.3
MK73-02	604.7459	391.6106	0.6476	0.0448	0.0032	0.0200	0.0006	0.0061	0.0003	131.4	4.1	130.8	9.3	126.1	5.4
MK73-03	631.8006	277.2858	0.4389	0.0525	0.0038	0.0189	0.0006	0.0065	0.0003	122.4	4.0	123.9	8.4	133.1	7.7
MK73-04	1660.2360	1948.2571	1.1735	0.0535	0.0031	0.0201	0.0006	0.0071	0.0003	131.9	4.0	137.6	8.0	149.7	6.9
MK73-05	759.1455	554.0223	0.7298	0.0609	0.0042	0.0189	0.0006	0.0067	0.0003	136.2	4.2	140.6	10.0	233.8	16.5
MK73-06	990.5897	487.6280	0.4923	0.0641	0.0044	0.0211	0.0007	0.0064	0.0004	135.5	4.3	140.1	9.9	131.2	7.5
MK73-07	6218.7149	8265.9259	1.3292	0.0675	0.0048	0.0196	0.0006	0.0092	0.0005	118.4	3.9	128.4	9.7	136.5	7.6
MK73-08	6158.7627	7967.6700	1.2937	0.0638	0.0031	0.0169	0.0005	0.0048	0.0002	134.6.	4.2	147.6	8.1	177.5	9.4
MK73-09	387.5459	183.9269	0.4746	0.0708	0.0060	0.0206	0.0007	0.0080	0.0005	123.0	4.1	130.4	10.1	141.9	9.0
MK73-10	319.8151	259.7931	0.8123	0.0714	0.0065	0.0229	0.0008	0.0090	0.0005	138.7	4.9	144.6	9.2	176.8	9.5
MK73-11	515.9108	289.9757	0.5621	0.0696	0.0053	0.0201	0.0006	0.0086	0.0004	128.3	4.2	132.9	8.4	173.2	9.5
MK73-12	321.4719	547.0613	1.7017	0.0763	0.0081	0.0205	0.0007	0.0069	0.0004	131.0	4.8	137.5	7.9	139.6	7.2
MK73-13	6462.5150	3992.7674	0.6178	0.0692	0.0038	0.0164	0.0005	0.0065	0.0019	132.4	4.7	138.5	10.8	160.8	9.7

reported to be syenitic-granitic rocks (Zhou et al., 2012a,b). In this study, we have found that the quartz syenite porphyry intruded (Fig. 14a) and disrupted the orebodies along clear intrusive contacts (Fig. 14b), and its formation was thus post-mineralization. This paper carried out regional geological mapping in Makou area in order to study the characteristics and forming mechanism of the ores (Fig. 3). Our field geology, optical microscopy, and EPMA analyses have identified that the albitite is the ore-hosting rock. The Makou biotite diorite contains up to 10.35% total Fe content (Table 4), and suggesting that it was responsible for the genesis of the ore.

6.2. Constraints from isotopic ages

In this study, the Makou iron mineralization was phlogopite Ar-Ar dated to be 130.76 ± 0.77 Ma, whereas the ore-forming biotite diorite and ore-hosting albitite were zircon U-Pb dated to be 131.2 ± 3.3 Ma and 129.6 ± 1.2 Ma, respectively. These ages are consistent (within the analytical uncertainties) with each other (ca. 130 Ma), further supporting that the biotite diorite was the ore-forming rocks.

Recent studies suggested that mineralization in the Luzong basin occurred mainly during the Zhuanqiao volcanic cycle (134.1 ± 1.6 Ma, Duan, 2009; Zhang et al., 2008; Zhou et al., 2010; Fan et al., 2014). The metallogeny may have commenced with the formation of the Panshiling volcanic-sedimentary-type iron deposit (ca. 134 Ma; coeval with the volcanic eruptive phase of the Zhuanqiao volcanic cycle), the following Yueshan Pb-Zn and Jingbian vein-type Cu deposits were formed at ca. 133–132 Ma. Soon after that (during the late Zhuanqiao volcanic cycleat ca. 130 Ma), porphyrite-related deposits (including Luohe, Nihe, Longqiao, Mabianshan, Yangshan, Daling and Dabaozhuang) were formed simultaneously with the Fanshan alunite deposit. Mineralization was weaker in the subsequent Shuangmiao volcanic cycle, during which only a series of A-type granite-related Au-U deposits were formed (ca. 123–126 Ma; Fan et al., 2008). Compared with other deposits in the Luzong basin (Table 7), it is seen that the Makou magnetite-apatite deposit was emplaced in albitite or intensely albite-altered biotite diorite, whereas the Luohe and Nihe deposits were emplaced in the Zhuanqiao Formation volcanics. The Makou iron ore formation is similar to Luohe and Nihe counterparts, and does not have genetic association with quartz syenite porphyry (ca. 127.3 ± 0.8 Ma) (Zhou et al., 2010).

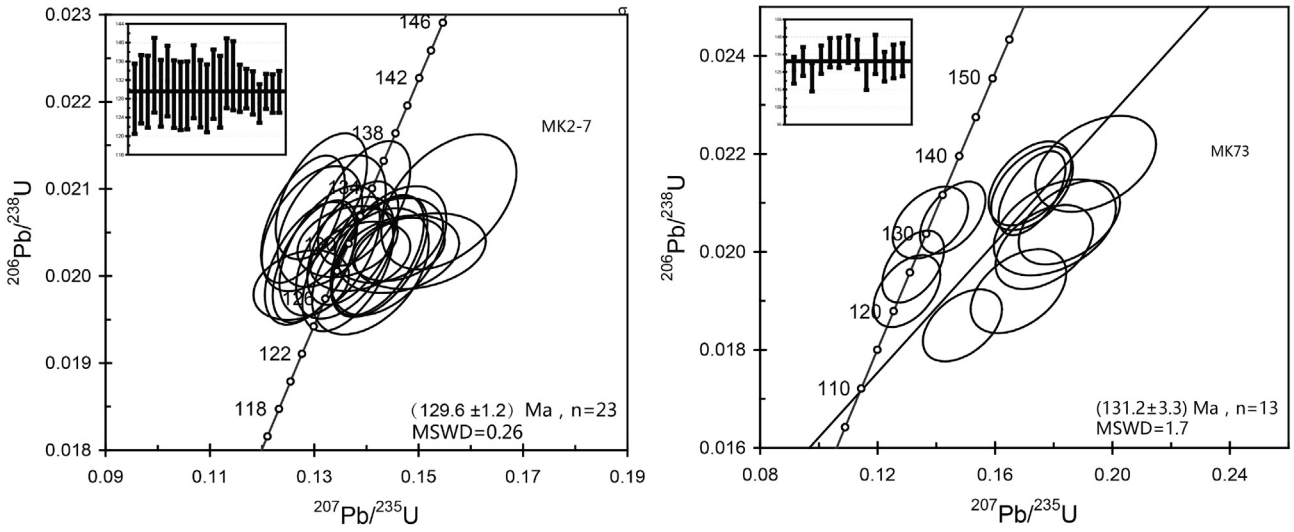

Fig. 12. Zircon U-Pb concordant diagrams for the Makou (left) albitite and (right) biotite diorite.

Table 6
^{40}Ar-^{39}Ar data for the Makou phlogopite.

Incremental heating	Temperature	^{36}Ar(a) [V]	^{37}Ar(ca) [V]	^{38}Ar(cl) [V]	^{39}Ar(k) [V]	^{40}Ar(r) [V]	Age (Ma)	± 2 s	^{40}Ar(r) (%)	^{39}Ar(r) (%)
6M43110D	81 °C	0.0000386	0.0001099	0.0000000	0.0049578	0.0368828	137.13	± 27.09	76.19	0.61
6M43111D	81 °C	0.0000526	0.0002580	0.0000094	0.0058337	0.0407281	128.98	± 24.20	72.17	0.72
6M43113D	82 °C	0.0000749	0.0002746	0.0000298	0.0132471	0.0965553	134.46	± 9.79	81.19	1.64
6M43115D	83 °C	0.0001299	0.0000280	0.0000270	0.0301418	0.2216122	135.59	± 4.77	85.10	3.72
6M43116D	84 °C	0.0000687	0.0001881	0.0000000	0.0189871	0.1388326	134.87	± 7.12	87.12	2.35
6M43117D	85 °C	0.0001975	0.0001409	0.0000614	0.0647989	0.4674904	133.13	± 2.35	88.79	8.00
6M43118D	86 °C	0.0003334	0.0005082	0.0001440	0.1730880	1.2401097	132.25	± 1.92	92.56	21.38
6M43120D	87 °C	0.0005288	0.0005460	0.0003297	0.3887731	2.7421159	130.26	± 0.67	94.55	48.02
6M43121D	88 °C	0.0000765	0.0003697	0.0000640	0.0549931	0.3895072	130.79	± 2.92	94.45	6.79
6M43122D	89 °C	0.0001249	0.0003791	0.0000557	0.0364576	0.2555258	129.47	± 4.40	87.26	4.50

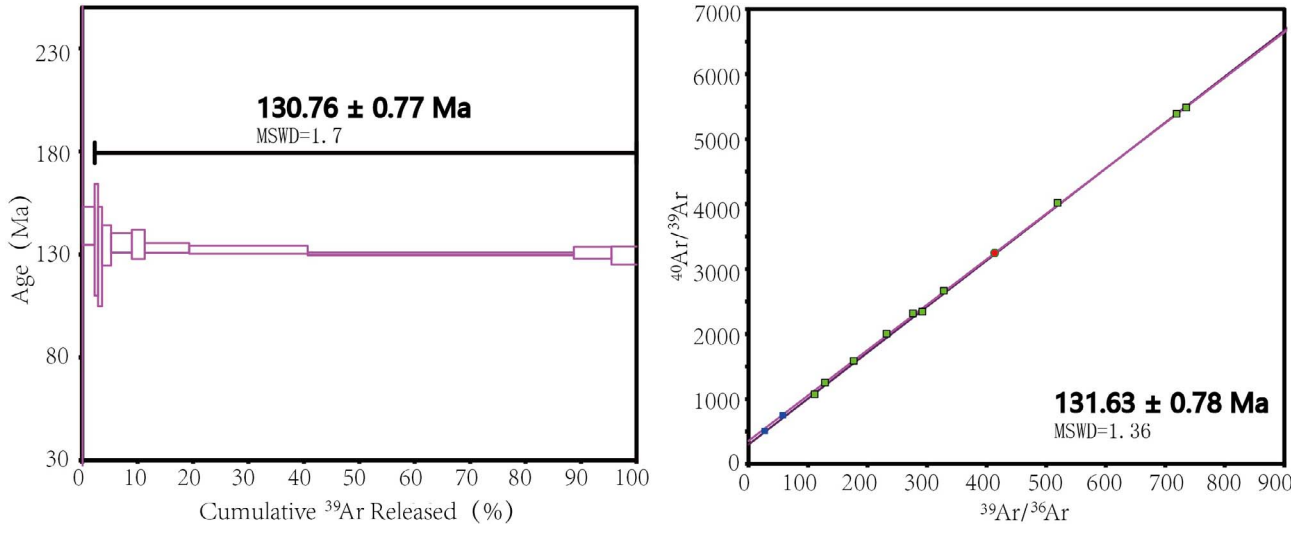

Fig. 13. ^{40}Ar-^{39}Ar spectrum and isochron age diagram for the Makou phlogopite.

6.3. Tectonic setting

The Makou iron mineral system (ca. 130 Ma) was formed in the late-stage of the Zhuanqiao volcanic cycle, which was broadly coeval with the shoshonitic magmatism (and associated metallogeny) in the continental volcanic basins of the MLYB (ca. 135–127 Ma; Zhou et al., 2010). We propose that during the late-stage of the Zhuanqiao volcanic cycle, the dioritic magma that intruded into the lower part of the Zhuanqiao Formation may have carried significant amounts of iron, sulfur and volatiles (e.g., H_2O, Cl_2, S_2, H_2S, SO_2, SO_3, H_2 and CO_2) (Knipping et al. 2015a; Knipping et al. 2015b, and Ningwu Iron Ore Research Group, 1978). The magma, after entering the shallow magma chamber(s), may have altered the Zhuanqiao volcanic country rocks. The albite growth rims around oligoclase in the biotite diorite indicating the gradual Na-enrichment in the residual magma, which produced strong sodic alteration of the biotite diorite and formed

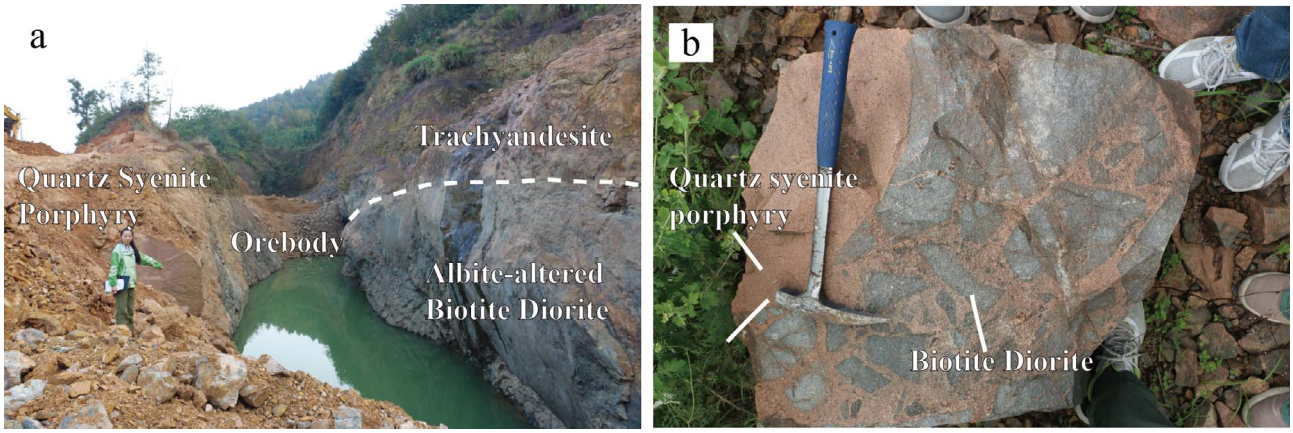

Fig. 14. Outcrop photographs of the Makou magnetite-apatite deposit.

Table 7
Summary of the nature of the iron mineralization of the major porphyrite-type Iron deposits in the Luzong basin.

Deposit	Luohe	Nihe	Makou
Occurrence	Zhuanqiao Fm. trachyandesite	Subvolcanic porphyrite	Albitite
Orebody	Vein, stockwork (upper part), breccia, massive, disseminated (lower part)	Veinlet-disseminated	Vein, disseminated, massive
Ore texture	Anhedral, medium-coarse-grained euhedral to subhedral	Fine-grained anhedral, medium-grained euhedral to subhedral	Anhedral, medium-grained euhedral to subhedral
Mineral assemblage	Di-Anh-Mag	Di-Anh-Mag	Mag-Ap-Di
Ore mineral alteration	Mag → Hem	Mag → Hem	Mag → Hem
Associated ore deposits	Gypsum, pyrite	Gypsum, pyrite	Nil
Wall rock alteration	Upper part: (dark color) Di- Anh-Mag, chl, epi, carbonate	Upper part: (light color) Q-Anh-Py	Upper part: (light color) Ser-Q-Tc
	Lower part: (light color) Q-Anh-Py	Lower part: (dark color) Di- Anh-Mag, chl, epi, carbonate	Lower part: (dark color) Di-Mag, commonly superimposed by chl and carbonate
Metallogenic age	130 Ma	131 Ma	127 Ma

massive albitite. The accumulation of hydrothermal fluids (with lower Na content due to its consumption by Na-alteration) may have led to the doming of the overlying wall rocks and fracture formation. The Fe, Ca, Mg and SiO_2 carried by the ascending fluids may have generated the Fe-Mg-Ca replacement, forming diopside, magnetite, ilmenite, apatite, biotite and phlogopite in the dark colored alteration zone at Makou. At the late stage of the fluid evolution, the fluid was extremely acidic and produced a wide range of light colored alteration (Ningwu Iron Ore Research Group, 1978). The decreasing temperature and involvement of meteoric water may have altered the early anhydrous alteration minerals (e.g., pyroxene) into hydrous ones (e.g., chlorite). The late stage alteration/mineralization features a paramagnetic mineral sequence of pyrite + chalcopyrite, followed by quartz + chlorite + minor hematite, and then eventually by calcite + dolomite + sericite + talc. The latter mineral assemblage makes up the light-color alteration zone at Makou.

Zhou et al. (2008) considered that the MLYB metallogeny could be divided into three stages, i.e., ca. 145–137 Ma (Fe-Cu-Au), ca. 135–127 Ma (Fe) and ca. 126 Ma (Cu-Pb-Zn-Au-U), and that there was a compressive-extensional tectonic transition at ca. 130 Ma. Mao et al. (2010) suggests that the Jurassic-Early Cretaceous magmatism was associated with the subduction of the Izanagi plate at a shallow angle or flat-slab subduction beneath the eastern China continent (Pirajno and Zhou, 2015). But the Early Cretaceous magmatism was related to lithospheric upwelling and partial melting of the lower crust, induced by a change in Izanagi plate motion parallel to the continent margin. These tectonic activities may have formed the volcanic basins and rifts in eastern China, and the associated intraplate magmatism and mineralization, including porphyry- and skarn-related and vein-type precious metal deposits (Mao et al., 2011). The post 130 Ma regional extension may have formed the post-orogenic A-/I-type granitoids and alkaline magmatic rocks .The change from regional compression to extension was suggested to be related to mantle upwelling, lower-crustal partial melting and basaltic under plating, and the Makou iron metallogeny may have been a product of this tectonic transition.

7. Conclusions

(1) The Makou iron mineralization in the Luzong basin is albitite-hosted, and comprises the albite alteration (Stage I), magnetite mineralization (Stage II), quartz-sulfide alteration (Stage III) and carbonate alteration (Stage IV) stages.
(2) The ore-hosting albitite and ore causative biotite diorite were zircon U-Pb dated to be 129.6 ± 1.2 Ma and 131.2 ± 3.3 Ma, respectively. Protoliths of the albitite may have been the biotite diorite, as both were formed at around 130 Ma and partial albite alteration of the latter was found close to the mine.
(3) Fluid inclusions from Stage II apatite homogenized at 252.2–322.6 °C (average 279 °C), whilst those from Stage III quartz homogenized at 120.1–189.2 °C (average 163.1 °C), all lower than the magnetite-apatite deposits or magnetite-apatite deposit in the Ningwu and Luzong basins.
(4) Makou is best classified as a magnetite-apatite deposit and the ore causative rock being biotite diorite, but not quartz syenite porphyry related as previously suggested.

Acknowledgements

This research was supported by funds from the National Natural Science Foundation of China (41320104003) and the National key Research and Development Program (grant no. 2016YFC0600206). We also thank our project partners East China Metallurgical Bureau of

Geology & Exploration for their valuable support during the fieldwork. The anonymous reviewers are thanked for greatly improving the manuscript through their thoughtful and thorough reviews.

References

Andersen, T., 2002. Correction of common lead in U-Pb analyses that do not report ^{204}Pb. Chem. Geol. 192, 59–79.

Badham, J.P.N., Morton, R.D., 1976. Magnetite-apatite intrusions and calc-alkaline magmatism Camsell River, N.W.T. Can. J. Earth Sci. 13, 348–354.

Belousova, E.A., Griffin, W.L., Shee, S.R., Jackson, S.E., O'Reilly, S.Y., 2001. Two age populations of zircons from the Timber Creek kimberlite, Northern Territory, as determined by laser-ablation ICPMS analysis. Aust. Earth Sci. 48, 757–765.

Black, L.P., Culson, B.L., 1978. The age of the Mud Tank carbonatite, Strangways Range, Northern Territory. Aust. Geophys. 3, 227–232.

Chang, Y.F., Liu, X.P., Wu, Y.C., 1991. The Copper-Iron Belt of the Middle and Lower Reaches of Yangtze River. Geol. Pub. House, Beijing pp. 1-380 (in Chinese).

Duan, C., 2009. Geological and geochemical characteristics and genesis of longqiao iron deposit in luzong basin, anhui, china (master dissertation). Hefei Univ. Technol. 1–261 (in Chinese with English abstract).

Dulski, P., 1994. Interferences of oxide, hydroxide, and chloride analyte species in the determination of rare earth elements in geological samples by inductively coupled plasma-mass spectrometry. Fresen. J. Anal. Chem. 304, 193–203.

Fan, Y., Liu, Y.N., Zhou, T.F., Zhang, L.J., Yuan, F., Wang, W.C., 2014. Geochronology of the Nihe deposit in the Lu-Zong basin and its metallogenic significances. Acta Petrol. Sin. 30 (5), 1369–1381 (in Chinese with English abstract).

Fan, Y., Zhou, T.F., Yuan, F., Qian, C.C., Lu, S.M., Cooke, D., 2008. LA-ICP-MS zircon U-Pb ages of the A-type granites in the Lu-Zong area and their geological significances. Acta Petrol. Sin. 24 (8), 1715–1724 (in Chinese with English abstract).

Fan, Y., Zhou, T.F., Yuan, F., Zhang, L.J., Qian, B., Ma, L., David, R.C., 2010. Geochronology of the diorite prophyrites in Ningwu basin and their metallogenic significances. Acta Petrol. Sin. 26 (9), 2715–2728 (in Chinese with English abstract).

Pirajno, F., Zhou, T.F., 2015. Intracontinental Porphyry and Porphyry-Skarn Mineral Systems in Eastern China: Scrutiny of a Special Case "Made-in-China". Econ. Geol. 110 (3), 603–629.

Ghasem, N., Majid, G., Majid, G., Farahnaz, D., Nematollah, R.O., 2012. Sorkhe-dizaj iron oxide-apatite ore deposit in the cenozoic alborz-azarbaijan magmatic belt. NW Iran. Resour. Geol. 63 (1), 42–56.

Geordie, G., Foster, D., 2000. Magmatic-hydrothermal albite-actinolite-apatite-rich rocks from the Cloncurry district, NW Queensland, Australia. Lithos 51, 223–245.

Knipping, J.L., Bilenker, L.D., Simon, A.C., Reich, M., Barra, F., Deditius, A.P., Lundstrom, C., Bindeman, I., Munizaga, R., 2015a. Supplementary Information for:" Giant Kiruna-type deposits form by 2 efficient flotation of magmatic magnetite suspensions". Geology 43 (7), 1–22.

Knipping, J.L., Bilenker, L.D., Simon, A.C., Reich, M., Barra, F., Deditius, A.P., Walle, M., Heinrich, C.A., Holtz, F., Mumizaga, R., 2015b. Trace elements in magnetite from massive iron oxide-apatite deposits indicate a combined formation by igneous and magmatic-hydrothermal processes. Geochim. Cosmochim. Acta 171, 15–38.

Koppers, A.A.P., 2002. ArArCALC-software for ^{40}Ar/^{39}Ar age calculations. Comput. Geosci. 28, 605–619.

Lee, J.Y., Marti, K., Severinghaus, J.P., Kawamura, K., Yoo, H.S., Lee, J.B., Kim, J.S., 2006. A redetermination of the isotopic abundance of atmospheric Ar. Geochim. Cosmochim. Acta 70, 4507–4512.

Li, W.T., 2015. Ore-forming fluids and ore genesis of continental subvolcanic magnetite-apatite deposits in ningwu and luzong area china (doctor dissertation). China Univ. Geosci. 1–204 (in Chinese with English abstract).

London, D., 1992. The application of experimental petrology of the genesis and crystallisation of granitic pegmatites. Can. Mineral. 30, 499–540.

Wolf, M.B., London, D., 1995. Incongruent dissolution of REE and Sr-rich apatite in peraluminous granitic liquids: Differential apatite, monazite, and xenotime solubilities during anatexis. Am. Mineral. 80 (7–8), 765–775.

Lu, H.Z., 1990. On Fluid-Melt Inclusions. Geochimica 3, 229–235 (in Chinese with English abstract).

Ludwig, K.R., 2003. Mathematical-statistical treatment of data and errors for ^{230}Th/U geochronology. Rev. Mineral. Geochem. 52 (1), 631–656.

Ma, F., Jiang, S.Y., Jiang, Y.H., Ni, P., Ling, H.F., 2006. Fluid inclusions and H-O isotopic compositions in the Washan and Dongshan iron deposits, Ningwu basin. China. Acta Petrol. Sin. 22 (10), 2581–2589.

Mao, J.W., Yu, J.J., Yuan, S.D., Chen, Y.B., Xie, G.Q., Hou, K.J., Xiang, J.F., Yang, Z.X., 2008. Iron oxide-copper-gold deposits: Characteristics, present research situation and ore prospecting. Mineral Deposits 27 (3), 267–278 (in Chinese with English abstract).

Mao, J.W., Xie, G.Q., Duan, C., Pirajno, F., Ishiyama, D., Chen, Y.C., 2011. A tectono-genetic model for porphyry-skarn-stratabound Cu-Au-Mo-Fe and magnetite-apatite deposits along the Middle-Lower Yangtze River Valley. Eastern China. Ore Geol. Rev. 43 (1), 294–314.

Mao, J.W., Xie, G.Q., Pirajno, F., Ye, H.S., Wang, Y.B., Li, Y.F., Xiang, J.F., Zhao, H.J., 2010. Late Jurassic-Early Cretaceous granitoid magmatism in eastern Qinling, central eastern China: SHRIMP zircon U-Pb ages and tectonic implications. Aust. Jour. of Earth Sci. 57, 51–78.

Ningwu, Iron, 1978. The Porphyrite Iron Deposit in Ningwu Area. Ore Research Group. Geol. Pub. House, Beijing pp. 1-197 (in Chinese).

Norrish, K., Chappell, B.W., 1977. X-ray fluorescence spectrometry. In: Physical Methods in Determinative Mineralogy, pp. 201–272.

Ren, Q.J., Liu, X.S., Xu, Z.W., 1991. Mesozoic volcano-tectonic depression and its mineralizing process in Luzong area. Anhui Province. Beijing: Geol. Pub. House 1–126 (in Chinese).

Renne, P.R., Balco, G., Ludwig, K.R., Mundil, R., Min, K., et al., 2011. Response to the comment by W.H. Schwarz,on "Joint determination of K-40 decay constants and Ar-40*/K-40 for the Fish Canyon sanidine standard, and improved accuracy for Ar-40/Ar-39 geochronology" by Renne et al. Geochim. Cosmochim. Acta 75, 5097–5100.

Renne, P.R., Mundil, R., Balco, G., Min, K., Ludwig, K.R., 2010. Joint determination of ^{40}K decay constants and ^{40}Ar*/^{40}K for the Fish Canyon sanidine standard, and improved accuracy for ^{40}Ar/^{39}Ar geochronology. Geochim. Cosmochim. Acta 74, 5349–5367.

Wiedenbeck, M., Alle, P., Corfu, F., Griffin, W.L., Meier, M., Oberli, F., Quadt, A.V., Roddick, J.C., Spiegel, W., 1995. Three natural zircon standards for U-Th-Pb, Lu-Hf, trace element and REE analyses. Geostand. Geoanal. Res. 19 (1), 1–23.

Williams, P.J., Barton, M.D., Johnson, D.A., Fontboté, L., de Haller, A., Mark, G., Oliver, N.H.S., Marschik, R., 2005. Iron oxide copper-gold deposits: geology, space-time distribution, and possible modes of origin. Econ. Geol. vol. 371-405 100thAnniversary.

Xie, X.J., Yan, M.C., Wang, C.S., Li, L.Z., Shen, H.J., 1989. Geochemical standard reference samples GSD 9–12, GSS - 8 and GSR 1–6. Geostandard. Newslett. 13 (1), 83–179.

Yuan, F., Zhou, T.F., Fan, Y., Zhang, L.J., Tang, M.H., Duan, C., Lu, S.M., Qian, C.C., 2008. Source, evolution and tectonic setting of Mesozoic volcanic rocks in Lozong basin. Anhui Province. Acta Petrol. Sin. 24 (8), 1691–1702 (in Chinese with English abstract).

Zhao, X.F., Zhou, M.F., 2011. Fe-Cu deposits in the Kangdian region, SW China: a Proterozoic IOCG (iron-oxide-copper-gold) metallogenic province. Mineral. Deposita 46, 731–747 (in Chinese with English abstract).

Zhai, Y.S., Yao, S.Z., Lin, X.D., 1992. Copper and Iron Deposits in Lower Yangtze River. Geol. Pub. House, Beijing pp. 1-145 (in Chinese).

Zhang, L.J., Zhou, T.F., Yuan, F., Fan, Y., 2008. SHRIMP U-Pb zircon dating of Yueshan intrusion in the Yueshan orefield, Anhui, and its significance. Acta Petrol. Sin. 24 (5), 1725–1732 (in Chinese with English abstract).

Zhang, L.J., Zhou, T.F., Fan, Y., Yuan, F., Qian, B., Ma, L., 2011. A LA-ICP-MS of Apatite from the Taocun Magnetite-apatite Deposit. Ningwu Basin. Acta Geol. Sin. 85 (5), 834–848 (in Chinese with English abstract).

Zhang, S., Wu, M.A., Wang, K., Li, X.D., Zhao, W.G., Wei, G.H., 2014. The Mineralization Related with the Syenite in Luzong Basin, Anhui Province. Acta Geol. Sin. 88 (4), 519–531 (in Chinese with English abstract).

Zhou, T.F., Fan, Y., Yuan, F., 2008. Advances on petrogensis and metallogeny study of the mineralization belt of the Middle and Lower Reaches of the Yangtze River area. Acta Petrol. Sin. 24 (8), 1665–1678 (in Chinese with English abstract).

Zhou, T.F., Fan, Y., Yuan, F., Song, C.Z., Zhang, L.J., Qian, C.C., Lu, S.M., David, R.C., 2010. Temporal-spatial framework of magmatic intrusions in Luzong volcanic basin in East China and their constrain to mineralizations. Acta Petrol. Sin. 26 (9), 2694–2714 (in Chinese with English abstract).

Zhou, T.F., Fan, Y., Yuan, F., Zhang, L.J., Ma, L., Qian, B., Xie, J., 2011. Petrogensis and metallogeny study of the volcanic basins in the Middle and Lower metallogenic belt. Acta Geol. Sin. 85 (5), 712–730 (in Chinese with English abstract).

Zhou, T.F., Fan, Y., Yuan, F., Zhong, G.X., 2012a. Progress of geological study in the Middle-Lower Yangtze river valley metallogenic Belt. Acta Petrol. Sin. 28 (10), 3051–3066 (in Chinese with English abstract).

Zhou, T.F., Song, M.Y., Fan, Y., Yuan, F., Liu, J., Wu, M.A., Qian, C.C., Lu, S.M., 2007. Chronology of the Bajiatan intrusion in the Luzong basin, Auhui, and its significance. Acta Petrol. Sin. 23 (10), 2379–2386 (in Chinese with English abstract).

Zhou, T.F., Wang, B., Fan, Y., Yuan, F., Zhang, L.J., Zhong, G.X., 2012b. Apatite-actinolite -magnetite deposit related to A-type granite in Luzong basin: Evidence from Makou iron deposit. Acta Petrol. Sin. 28 (10), 3087–3098 (in Chinese with English abstract).